https://doi.org/10.5194/wes-2021-104
Preprint. Discussion started: 7 October 2021

Open Access
WIND ENERGY SCIENCE
DISCUSSIONS

Vortex identification methods applied to wind turbine tip vortices

Rodrigo Soto-Valle[1], Stefano Cioni[2], Sirko Bartholomay[1], Marinos Manolesos[3], Christian Navid Nayeri[1], Alessandro Bianchini[2], and Christian Oliver Paschereit[1]

[1]Technische Universität Berlin, Hermann-Föttinger Institut, Müller-Breslau-Straße 8,10623 Berlin, Germany
[2]Università degli Studi di Firenze, DIEF, via di Santa Marta 3, 50139 Firenze, Italy
[3]College of Engineering, Swansea University, Bay Campus, Fabian Way, Swansea, SA1 8EN, UK

Correspondence: Rodrigo Soto-Valle (rodrigo.soto@campus.tu-berlin.de)

Abstract. This study describes the impact of postprocessing methods on the calculated parameters of tip vortices of a wind turbine model when tested using Particle Image Velocimetry (PIV). Several vortex identification methods and differentiation schemes are compared. The chosen methods are based on two components of the velocity field and its derivatives. They are applied to each instantaneous velocity field from the dataset and also to the calculated average velocity field. The methodologies are compared through the vortex center location, vortex core radius and jittering zone.

Results show that the tip vortex center locations and radius have good comparability and can vary only a few grid spacings between methods. Conversely, the convection velocity and the jittering surface, defined as the area where the instantaneous vortex centers are located, vary between identification methods.

Overall, the examined parameters depend significantly on the postprocessing method and selected vortex identification criteria. Therefore, this study proves that the selection of the most suitable postprocessing methods of PIV data is pivotal to ensure robust results.

1 Introduction

The wake of a wind turbine is characterized by the presence of vortex structures. Two types of concentrated vortices can be identified, which are shed from the root and the tip region. The latter form strong helical shapes that influence the wake of the wind turbine.

The tip vortices are generated by the pressure difference between the top and lower side of the blade tip, which lead to a flow the pressure side to the suction side of the blade (Karakus et al., 2008; Sherry et al., 2013b). In this way, the tip vortices of a wind turbine represent a source of noise (Arakawa et al., 2005) and energy loss (Shen et al., 2005). Moreover, the wake development needs proper consideration in the layout of a wind park (Marten et al., 2020), as it can affect the performance of wind turbines located downstream. Therefore, a more detailed characterization of the wind turbine wake vortices does represent a relevant research topic.

Since the first introduction of Particle Image Velocimetry (PIV) applied to wind turbine aerodynamics by Smith et al. (1990), a number of experimental investigations have been performed and a variety of methods have been employed to identify the vortex center and other characteristics. Yang et al. (2012) studied the formation and evolution of helical tip vortices of a wind turbine model under atmospheric boundary layer wind. It is shown, by using the vorticity to identify the vortices, a high variation in the position of the tip vortices. This effect is known as wandering or jittering and it is related to turbulence, vibrations of the model turbine (e.g. blades and tower) and the PIV system. Additional investigations (Maalouf et al., 2009; Soto-Valle et al., 2020) show the same effect using different identification methods such as the Q-criterion or circulation-based methods.

Micallef et al. (2014) studied the mechanism of the initiation of the tip vorticity in a wind turbine. The findings showed how the vorticity convects and forms a unique and symmetrical tip vortex behind the trailing edge. The location of the vortex center, identified by the maximum vorticity value, was found to be slightly inboard the rotor.

Sherry et al. (2013a) studied tip vortices from a wind turbine in a water channel. The results highlighted the breakdown of the wake due to the mutual interaction between helical structures of the tip vortices, which is highly dependent on the tip speed ratio. Additionally, the jittering of the tip vortices was also detected.

Ostovan et al. (2019) studied the effect of winglets on the tip vortices. The results showed that the winglets cause faster downstream convection and a radially outward motion of the tip vortices, thus more wake expansion. The tip vortex was characterized by means of the velocity field when the convection velocity is subtracted, i.e. the vortex-induced velocity field, and the center was identified where the velocity is zero.

In summary, several vortex identification methods (VIM) have been employed so far. Yet, a common methodology for the identification of vortices in the wake of a wind turbine has not been defined, as shown in Table 1. Furthermore, some investigations do not provide the complete implementation methodology, thus hindering an extensive comparison between methods.

Table 1. Wind turbine tip vortices studies employing the PIV technique and VIM details.

contributor	test facility^a	diameter	VIM	scheme
Middle East TU, Ostovan et al. (2019)	WT, open jet	$0.94m$	zero induced velocity	central difference
Iowa SU, Yang et al. (2011, 2012)	WT, closed-loop	$0.25m$	vorticity magnitude	not specified
TU Delf, Micallef et al. (2014, 2011)	WT, open-jet	$2m$	vorticity magnitude	central difference
ENSAM, Maalouf et al. (2009)	WT, closed-loop	$0.5m$	circulation	integration
Edinburgh U, Whale et al. (2000)	WC	$0.175m$	vorticity magnitude	fifth order polynomial
Wright SU, Ning and Yang (2013)	WT, open-jet	$0.25m$	vorticity magnitude	not specified
TU Berlin, Soto-Valle et al. (2020)	WT, closed-loop	$3m$	Q-criterion	central difference
FLAIR, Sherry et al. (2013b, a)	WC	$0.23m$	swirling strengh criterion	Richarson extrapolation

(a) WT: wind tunnel, WC: water channel.

This paper aims at comparing different vortex identification methods to evaluate their suitability to study the tip vortices of a wind turbine. The methods are applied to velocity field planes that were obtained through PIV in the near wake of a wind turbine model located in a wind tunnel facility (Soto-Valle et al., 2020). The comparison between methods and schemes is done by means of vortex center location, vortex core radius and jittering zone. In total three different VIMs are compared: vorticity, Q-criterion and Graftieaux. The first two VIMs require differentiation, thus, the application of six different schemes is examined.

The following section, Sect. 2, gives the mathematical overview of the methods to identify vortices and the differentiation schemes applied on their implementation. Subsequently, the wind tunnel and test rig used to generate the experimental dataset are introduced in Sect. 3, followed by the methodology in Sect. 4. The results are presented in Sect. 5 to conclude with the most important remarks in Sect. 6.

2 Vortex identification methods

Many vortex identification methods have been proposed in the literature (Spalart, 1988; Hunt et al., 1988; Graftieaux et al., 2001; Vétel et al., 2010; Liu et al., 2016; Shkarayev and Kurnosov, 2017; Zhang et al., 2018a, b; Liu et al., 2020). In this work, three identification methods are compared. The chosen methods are based on the velocity field U, differing in their derivative orders. Consequently, the methods are based on the velocity field (U) and first-order derivatives (∇U). The selected methods are:

- Graftieaux's method, Graftieaux et al. (2001)
- Vorticity magnitude, Spalart (1988)
- Q-criterion, Hunt et al. (1988)

Additional methods can be derived from the eigenvalue analysis, such as λ_2, Δ or swirling strength criteria (Zhang et al., 2018b). However, for the scope of this research, they represent similar approaches and therefore, only the selected methods are analysed.

A full description of the selected methods is given below. For a more extensive review of VIMs, the interested reader is directed to Zhang et al. (2018b).

2.1 Graftieaux's method

This method identifies the vortex through a global quantity, Γ_1, from an equivalent solid-body rotation. This function allows to determine the location of the vortex center. Equation 1 shows the scalar, Γ_1, defined in a discrete space.

$$\Gamma_1 = \frac{1}{N}\sum_S \frac{(\overrightarrow{PM}\cdot U_M)\cdot z}{||\overrightarrow{PM}||\;||U_M||} = \frac{1}{N}\sum_S sin(\theta_M), \tag{1}$$

where P is a fixed point to evaluate, U_M is the velocity of the M surrounding points to P in the surface S, $\overrightarrow{PM}$ is the radius vector that connects the point P with M, N is the total number of points considered in the surrounding of P, and z is the unit vector, normal to the surface plane S.

Figure 1 shows a graphic representation of the parameters for the calculation of Γ_1. Over a two-dimensional frame, Γ_1 represents the topology of the surrounding flow to the point P. In this way, Γ_1 is the average contribution of the angles between the velocity U_M and the radius vector. Therefore, at the vortex center, the value of Γ_1 tends to be close to the unity because the velocity contribution is perpendicular to the radius vector.

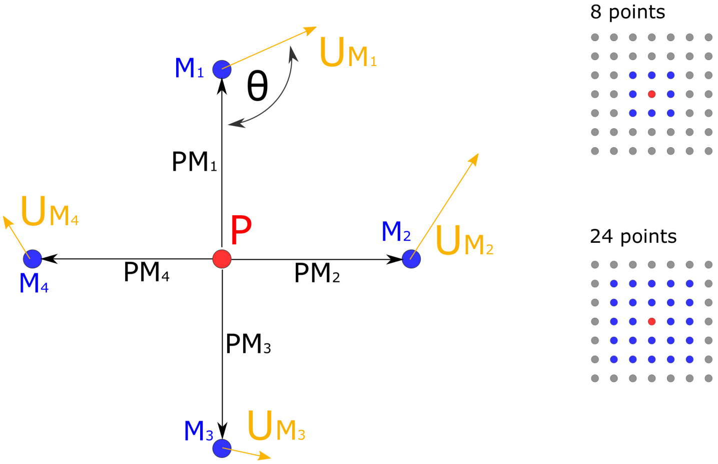

Figure 1. Sketch of Graftieaux parameters in Γ_1 implementation.

Depending on the grid size, the value of Γ_1 might not reach unity as the center of the vortex could not be located on a grid point. Therefore, the vortex center is estimated as the position of the maximum value of Γ_1.

2.2 Vorticity magnitude

The vorticity is defined as the curl of the velocity field as show in Eq. 2

$$\omega = \nabla \times U \overset{2D}{=} \frac{\partial v}{\partial x} - \frac{\partial u}{\partial y}, \tag{2}$$

where ω is the vorticity. Equation 2 shows also a two-dimensional representation, where the out of plane vorticity is a function of the velocity field $U = U(u(x,y), v(x,y)) \equiv U(x,y)$.

In this way, the vorticity quantifies how the velocity vector changes when it moves in a direction perpendicular to it and therefore, is a natural candidate for vortex identification. Indeed, this method has been used for a long time (Spalart, 1988). In the vortex core, the vorticity is predominant compared to the shear rate deformation, due to the rotation of the fluid. Hence, the vortex core is identified as a region of high vorticity. At the vortex center, the vorticity reaches its maximum value. Consequently, the maximum value of vorticity can be used to locate the vortex center. However, as it has been pointed out by many authors (Liu et al., 2019; Zhang et al., 2018a), vorticity cannot distinguish between parallel shear motion and vortical motion. As an example, a laminar boundary layer shows high vorticity even though no vortical motion is present. Moreover, a vorticity threshold must be chosen to plot the vorticity iso-surfaces and the determination of the vortex core radius relies on other quantities such as the swirl velocity. Nevertheless, this method is based on first-order derivatives, which are easy to implement and commonly used in the literature.

2.3 Q-criterion

The most common vortex identification methods are based on the analysis of the velocity gradient ∇U. For instance, from the analysis of the eigenvalues of ∇U, Eq. 3, three invariants can be found ($P,\ Q,\ R$)

$$\lambda^3 + \lambda^2 P + \lambda Q + R = 0, \tag{3}$$

In particular, the second invariant Q can be obtained through:

$$Q = \frac{1}{2}\left(tr\,(\nabla U)^2 - tr((\nabla U)^2)\right) \overset{2D}{=} -\frac{1}{2}\left(\left(\frac{\partial u}{\partial x}\right)^2 + \left(\frac{\partial v}{\partial y}\right)^2\right) - \frac{\partial u}{\partial y}\frac{\partial v}{\partial x}, \tag{4}$$

where tr is the mathematical trace. In this way, the second invariant, Eq. 4, defines the Q-criterion. The method can be interpreted as the difference between the vorticity magnitude and the magnitude of the strain rate (Kolář, 2007). Hence, similar to the vorticity magnitude, the vortex core will be characterized by positive large magnitudes of Q since the rotation of the fluid is predominant compared to the strain rate in this region. In addition, areas characterized by parallel shear motion, without rotation, will not be identified as a vortex ($Q < 0$) and therefore, overcoming one of the limitations of the use of vorticity in vortex identification. Nevertheless, a threshold is still needed in order to determine the core region.

2.4 Differentiation schemes

As shown in the previous section, several vortex identification methods are based on the gradient of the velocity field, then inherently the evaluation of flow field derivatives is necessary. In this way, the differentiation of the velocity fields from either computational data or experimental techniques (as PIV) is needed. Both normally come in a discrete format.

In case of PIV data, the choice of the differentiation scheme becomes more relevant due to the presence of noise affecting the measurements. Noise sources include optical distortion, light sheet non-homogeneity, transfer function of CCD and particle characteristics, among others (Foucaut and Stanislas, 2002). Indeed, the process of differentiation can amplify the effects and therefore compromise the results.

Many methods have been developed to calculate spatial derivatives from discrete data. The most frequently used methods are based on discrete differential operators applied to the surrounding points of the position to evaluate (Foucaut and Stanislas, 2002). In this way, the formulation of these schemes can be obtained through Taylor expansion. Equation 5 shows a generalization of the derivative scheme application on a function f over the dimension x in the point j (Raffel et al., 2018).

$$\left.\frac{\partial f}{\partial x}\right|_i = f_i' + \sum_{p=n+1}^{\infty} \alpha_p \frac{\Delta x^{p-1}}{p!}\left.\frac{\partial^p f}{\partial x^p}\right|_i + \epsilon\frac{\sigma_f}{\Delta x}, \tag{5}$$

where Δx is the grid spacing. The first term, on the right side, represents the implementation scheme (see Table 2). The following term is the truncation error, which depends on the number of elements from the Taylor expansion (n) (LeVeque, 1998). Subsequently, the values of α_p are obtained through finite Taylor expansion. The last term on the right is the noise error (or uncertainty in Table 2), ϵ is the noise amplification coefficient and σ_f is the measurement noise level which could be estimated from the uncertainty from the measurements (Lourenco and Krothapalli, 1995). Accordingly to Foucaut and Stanislas (2002), there is a trade-off between the truncation error and the noise amplification, therefore, the increment of the order will increase the uncertainty of the scheme.

The backward, central and forward differencing schemes provide the simplest implementation. Nevertheless, additional schemes have been studied with the purpose of either increasing the accuracy or reduce the uncertainty of the results. Raffel et al. (2018) presented, for example, the Richarson extrapolation which applied a fourth-order ($n = 4$) central differentiation scheme. Another tested methodology shown in the same work is the least-squares scheme, a second-order scheme, designed to minimize noise propagation. However, this approach has the tendency to smooth the estimation of the derivative because the outer data is weighted more than the inner data.

The latter schemes are defined for a single variable function and applied in one dimension at a time. Conversely, the velocity field can be influenced by the complete spatial coordinates. Therefore, the velocity gradient should depend on the surrounding flow. Raffel et al. (2018) proposed then, the circulation scheme that accounts for the effect of the surrounding flow (see Table 2). The first derivative is expressed as a central difference of derivatives in the other direction. This method reduces noise compared to the central difference scheme since the velocities of six neighboring points are considered instead of two.

Table 2 shows a summary of the mentioned schemes with their accuracy and uncertainty.

Table 2. Summary of differentiation schemes and implementation^a.

Operator	Implementation f_i'	Accuracy	Uncertainty, ϵ
Forward difference, FD	$\frac{f_{i+1}-f_i}{\Delta x}$	$\mathcal{O}(\Delta x)$	1.41
Backward difference, BD	$\frac{f_i-f_{i-1}}{\Delta x}$	$\mathcal{O}(\Delta x)$	1.41
Richarson extrapolation, RE	$\frac{f_{i-2}-8f_{i-1}+8f_{i+1}-f_{i+2}}{12\Delta x}$	$\mathcal{O}(\Delta x^4)$	0.95
Central difference, CD	$\frac{f_{i+1}-f_{i-1}}{2\Delta x}$	$\mathcal{O}(\Delta x^2)$	0.7
Circulation based method, CM	$\frac{f_{CD}\|_{i,j-1}+2f_{CD}\|_{i,j}+f_{CD}\|_{i,j+1}}{4}$	$\mathcal{O}(\Delta x^2)$	0.6
Least squares, LS	$\frac{2f_{i+2}+f_{i+1}-f_{i-1}-2f_{i-2}}{10\Delta x}$	$\mathcal{O}(\Delta x^2)$	0.32

(a) Composed from Raffel et al. (2018), Foucaut and Stanislas (2002) and van der Wall and Richard (2006).

3 Experimental dataset

The analysis shown in the rest of this paper relies on the stereo-PIV-dataset from previous work by Soto-Valle et al. (2020). In the following, the experimental setup is presented.

The experiments were carried out in the closed-loop wind tunnel at the Technische Universität Berlin. The wind turbine model, Berlin Research Turbine (BeRT) (Pechlivanoglou et al., 2015), was located in the large test section, with a cross-sectional area of $4.2 \times 4.2\ m^2$. The freestream velocity was set to $u_\infty = 6.5\ ms^{-1}$ and the rotational speed to $f = 3\ Hz$. Figure 2 shows the facility and test rig.

BeRT is a three-bladed, upwind horizontal axis wind turbine model with a rotor diameter of $D = 3\ m$. The blades were twisted, tapered, and based on Clark Y airfoil profile along the full span. The Reynolds number was in the range of $Re = 1.7 - 3.0 \times 10^5$ based on the chord length and the operational conditions.

The velocity field was measured using a stereo-PIV system, consisting of a Quantel Dual-Nd:Yag double laser with energy of $171 mJ$, a mirror arm, the laser sheet optics, two 14bit PCO 2000 cameras with a CCD-chip resolution of 2048×2048 pixel, and an ILA synchronizer connected to the measurement computer.

The measurement plane was horizontal and was centered at the tip location when the blade was in the horizontal position. For the purpose of this study, one vortex age was chosen at $\phi = 40°$. This provides a total of 1200 recorded image pairs in a phase-locked position. The image postprocesing was done with the software PIVview3C (PIVTec GmbH), resulting in a field of view of $435 \times 435\ mm^2$ and a spatial resolution of $\Delta x = \Delta y = 3.6\ mm$.

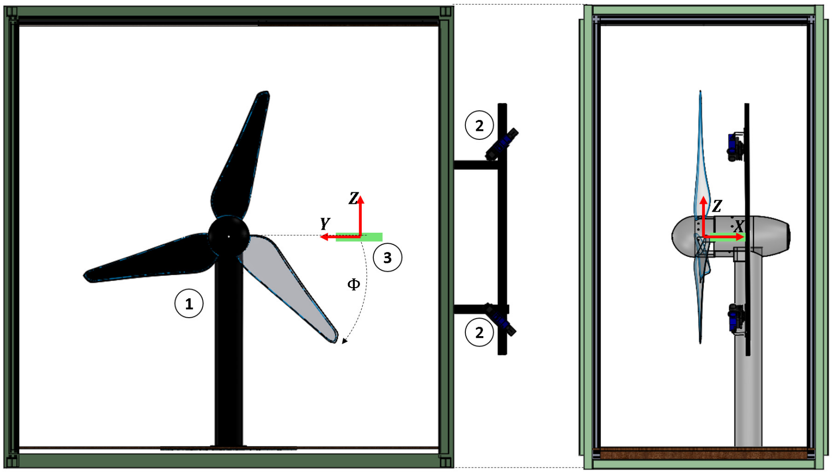

Figure 2. Front and lateral sketch of Berlin Research Turbine ① (BeRT), cameras ② and laser sheet ③ (Soto-Valle et al., 2020).

4 Methodology

A two-dimensional analysis is carried out on the dataset. To conduct a three-dimensional analysis of the vortex structures, additional parallel planes are needed. Therefore, only the two in-plane velocity components are used ($x-y$), even though the out of plane velocity w is available from the stereo-PIV measurements.

The application to obtain the vortex properties follows, while the statistical analysis of the available data is described at the end of this section.

4.1 Vortex center and convection velocity

The velocity fields are analyzed through the application of the VIMs described in Sect. 2. In the case of the vorticity magnitude and Q-criterion, VIMs are implemented using the differentiation schemes shown in Table 1. In the case of Graftieaux's method, which does not use the derivatives of the velocity field, two amounts of surrounding points are considered (8- and 24-points, see Fig. 1).

Figure 3 shows a flowchart of the methodology used in this study. In this way, a dataset of velocity fields ($N = 1200$), from the PIV measurements is available. Both the average and the instantaneous flow fields are analyzed to identify the vortex center location, (x_c, y_c), by means of the position of the maximum value of each VIM parameter (Γ_1, ω, Q).

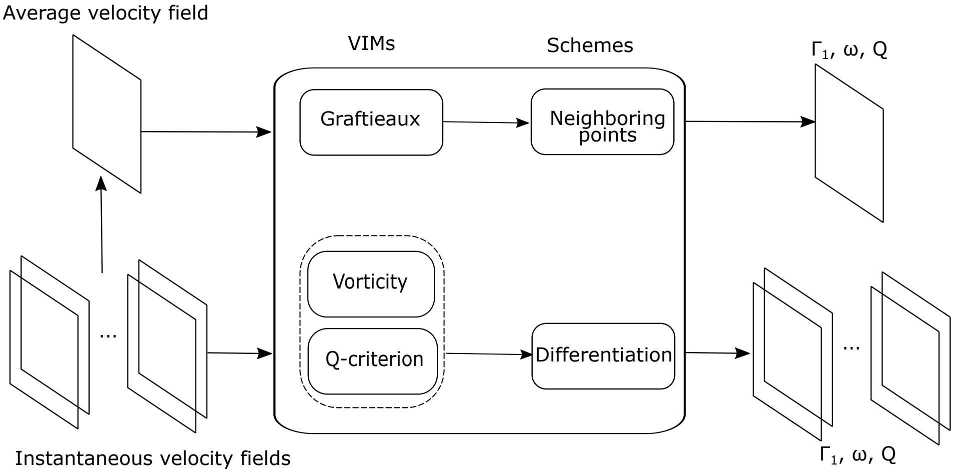

Figure 3. Flowchart of the implementation of the vortex identification methods and schemes.

Results are presented in a normalized form and bounded by the unity. In the case of Γ_1, the parameter already fulfill these requirements by its definition, while the results of vorticity and Q magnitudes are normalized according to Eq. 6:

$$\boldsymbol{\omega} = \frac{\omega}{\omega_{max}}, \boldsymbol{Q} = \frac{Q}{Q_{max}}, \tag{6}$$

where ω_{max} and Q_{max} are the overall vorticity and Q absolute maximum magnitudes. Moreover, the calculated distributions are presented in a reduced area of interest, as depicted in Fig. 4.

https://doi.org/10.5194/wes-2021-104
Preprint. Discussion started: 7 October 2021

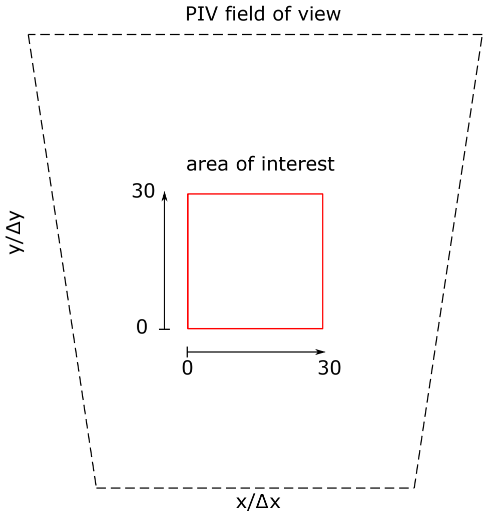

Figure 4. Field of view of PIV measurements and area of interest of the current study. Axes are normalized by the grid spacing.

After the shedding from the tip, the tip vortex is both translating and rotating at the same time. Considering this, the convection velocity (downstream, x and outboard directions, y) is estimated as the velocity magnitude corresponding to the vortex center location. The latter is a common estimation in the literature (van der Wall and Richard, 2006; Yamauchi et al., 1999). Therefore, the estimation is also affected by both the VIM and the scheme chosen on their application.

4.2 Core radius

The core radius is calculated using the following steps:

1. The induced velocity field U', Eq. 7, is obtained by means of the subtraction of the convection velocity from the velocity field. The resulting velocity field is characterized by presenting the induced contribution only.

$$U'(x,y) = U(x,y) - U(x_c,y_c). \tag{7}$$

2. The swirling velocity is analyzed through vertical and horizontal lines using the vortex center as an origin reference. The study is done in both directions to check the symmetry of the vortex, as vortices can have asymmetric shapes (Skinner et al., 2020).

$$U_{\theta,x} = U'(x, y = y_c); \quad U_{\theta,y} = U'(x = x_c, y). \tag{8}$$

3. A spline line is fitted to the swirling velocity curves. The radius, r_c, is estimated as half the distance between the maximum values of the fit curve.

https://doi.org/10.5194/wes-2021-104
Preprint. Discussion started: 7 October 2021

The procedure is repeated for each VIM and scheme and applied to both the average and the instantaneous velocity fields. Figure 5 shows the instantaneous induced velocity, $v(x,y)$ of a representative PIV velocity field and the corresponding swirling velocity.

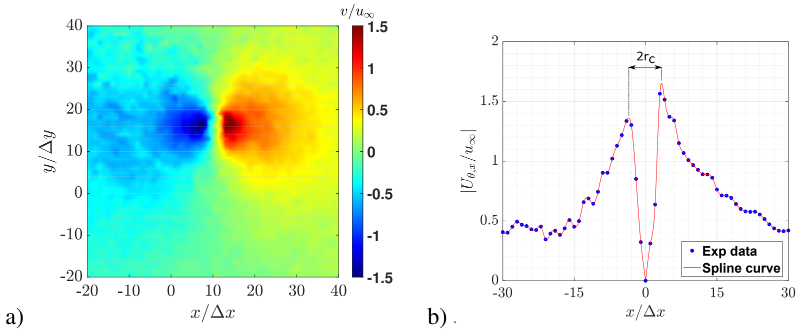

Figure 5. a) Induced velocity field $v(x,y)$. b) Swirling velocity with the x-axis shifted to the corresponding vortex center.

Both vortex characteristics, convection velocity and core radius, are normally used to describe the evolution of the vortex at different ages (Snel et al., 2007; Nilsson et al., 2015) as well as a parameter to quantify induced drag penalties from the tip vortices (Ostovan et al., 2019).

4.3 Statistical analysis

A statistical analysis is made over the complete dataset of the instantaneous velocity fields. In this way the vortex center, the convection velocity and the core radius are analyzed in terms of their location and magnitude variations.

An ellipse is used to define the jittering characteristic zone, similar to the work of Sherry et al. (2013b). The semi-axes of the ellipse a and b are defined to include all vortex center locations and the overall surface of the ellipse is calculated as $S = \pi ab$.

5 Results

The results are presented as follows. First, an overview of the VIMs and schemes applied to the average velocity field are shown using the vortex center locations and convection velocities based on the three identification parameters Γ_1, $\boldsymbol{\omega}$, $\boldsymbol{Q}$. The subscripts provide the information about the scheme implementation, e.g, $\boldsymbol{\omega_{CD}}$ shows the results from vorticity using the central difference scheme.

Second, a statistical analysis of the complete set of instantaneous velocity fields is performed. In this way, the location of the vortex center locations is studied in order to define the shape, distribution and surface of the jittering zone described by each VIM and scheme. Additionally, these results are used to compare the scattering of the convection velocities and core radii.

5.1 Average velocity field

Figure 6 shows the magnitude distribution of the parameter Γ_1 after the application of Graftieaux's method with 8- and 24-points on the average velocity field. Both cases show a concentration of the magnitude in a core with one peak in the same location at $(x/\Delta x, y/\Delta y) = (11, 14)$ and with an almost identical magnitude of $\Gamma_1 \approx 0.97$, although the $24-$p scheme extends its distribution over a larger zone.

Graftieaux's method has been developed for stationary vortices, while indeed, the test case is a superposition of the vortex-induced velocities and the streamwise flow, which convects the vortex downstream. The latter difficulty is overcome by subtracting the background velocity. Sherry et al. (2013b) proposed subtracting the average phase-locked velocity, $\overline{U}$ obtained by averaging each magnitude, streamwise (u) and lateral (v) from the full field of view.

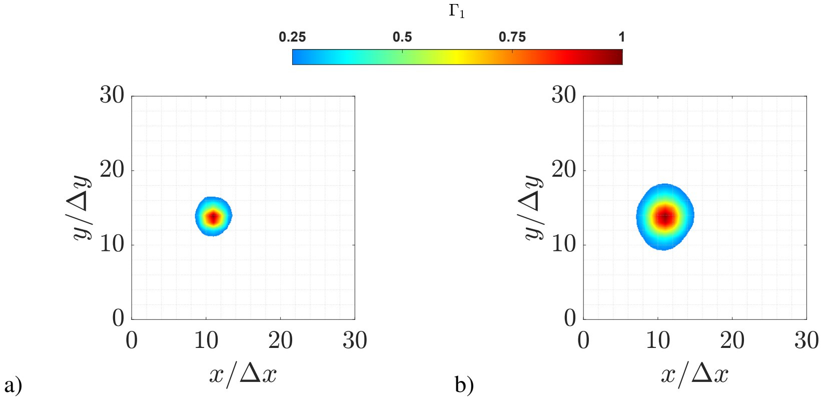

Figure 6. Γ_1 magnitude on the area of interest, where the methodology is applied after removing the average velocity from the field of view. a) $8-$points. b) $24-$points.

Figures 7 and 8 depict the results from the vorticity and Q-criterion, respectively. In contrast to Γ_1, The application of $\boldsymbol{\omega}$ and $\boldsymbol{Q}$ VIMs is not dependent on the subtraction of the background flow, so this step is not performed for these two methods.

Vorticity and Q-criterion provide almost identical results with a concentrated region defining the vortex, as apparent in Figs. 7 and 8. Nevertheless, in case of BD, CD, FD and RE schemes (Figs. 7 and 8, a-d) the vortex cores do not exhibit a unique peak in their center. Instead, the vortex is characterized by high radially distributed magnitude and multiple local maxima can be identified ($\boldsymbol{\omega} \geq 0.8$). Furthermore, in the center of the core, the magnitude is lower than the perimeter. The scheme cases LS and CM (Figs. 7 and 8 e-f) exhibit a smoother distribution compared to the other schemes. A unique maximum is found closer to the center of the vortex core in each case.

The presence of the multiple maxima and the ring-like distribution of the parameters $\boldsymbol{\omega}$ and $\boldsymbol{Q}$ can be explained through different hypotheses. On the one side, the cause could be the level of noise in the vortex core because of the lack of seeding (Foucaut and Stanislas, 2002; van der Wall and Richard, 2006). The rotational motion of the fluid causes the seeding particles to be pushed at the edges of the vortex. For this reason, the velocity vectors shall be evaluated through interpolation, introducing a further source of uncertainty in the results. In this way, the contours of $\boldsymbol{\omega}$ and $\boldsymbol{Q}$ have a single peak concentration for

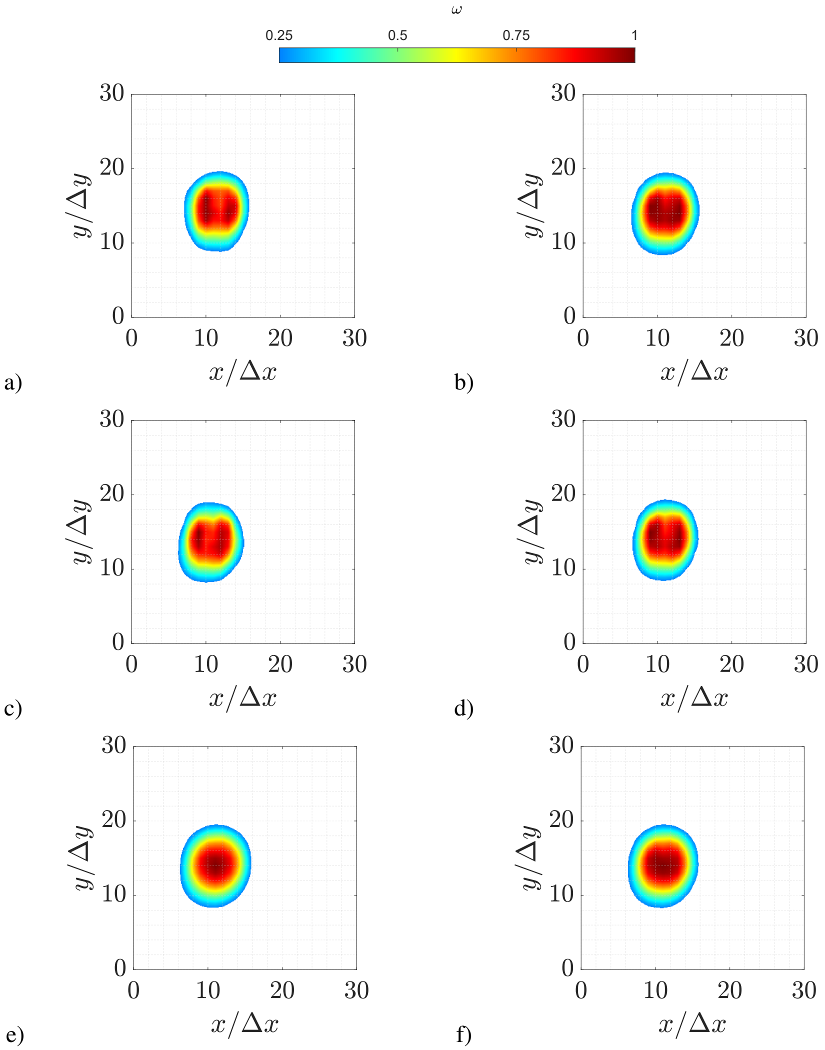

Figure 7. Normalized vorticity magnitude on the area of interest. a) Backward difference. b) Central difference. c) Forward difference. d) Richardson extrapolation. e) Least square. f) Circulation method.

the schemes with the lowest uncertainties (LS and CM) while two peak concentrations appear for the schemes with higher uncertainty (CD, RE, BD and FD).

On the other side, the presence of multiple maxima might also be due to small-scale structures within the vortex, as suggested by Bonnet (1998). It is conceivable that these structures are originated during the shedding of the tip vortex from the blade. Certainly, the pressure difference between the pressure and suction sides of the blade is only one of many effects that take part in the formation of the tip vortices. Several experiments show that the flow at wingtips involves the interaction of multiple vortices, shear layer instabilities, flow separation and re-attachment (Giuni and Green, 2013a; Devenport et al., 1996; Micallef,

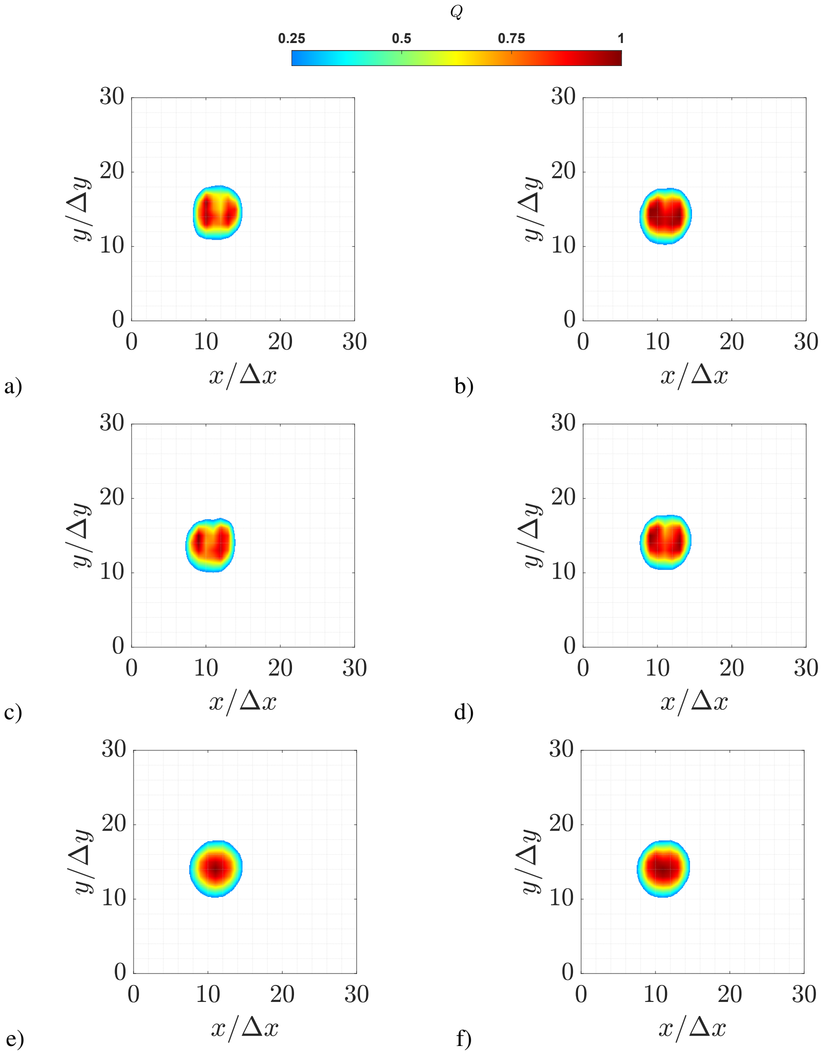

Figure 8. Normalized Q-criterion magnitude on the area of interest. a) Backward difference. b) Central difference. c) Forward difference. d) Richardson extrapolation. e) Least square. f) Circulation method.

2012). The involved structures are also affected by the blade shape, tip geometry, Reynolds number, and load distribution (Giuni and Green, 2013a) and generally merge into a single structure.

In conclusion, the multiple peaks could be caused by the uneven shedding of vorticity in the chordwise direction. In the work of Micallef et al. (2014) that shows the formation of the tip vortices in a horizontal axis wind turbine, a complex vorticity distribution along the blade chord is observed, which seems to cause multiple vorticity peaks inside the core. These multiple peaks can be identified in the vortex core even after the tip vortex has been shed from the blade. In the present results, the same effect is obtained when the high uncertainty schemes are applied (CD, RE, BD and FD).

Overall, some VIMs and schemes lead to different interpretations of the results. In fact, Graftieaux distribution together with vorticity and Q-criterion magnitudes employing LS and CM schemes are characterized by the presence of a single peak, in contrast with the rest of the schemes with the presence of several maxima within small structures are found.

Regarding the position of the vortex centers, the locations are shown in Fig. 9, overlapped with the vorticity magnitude distribution. It can be seen that the identification method does not have a strong influence on the estimation of the vortex center location with differences up to $y/\Delta y = 2$ and $x/\Delta x = 4$ grid steps in the lateral and streamwise directions, respectively.

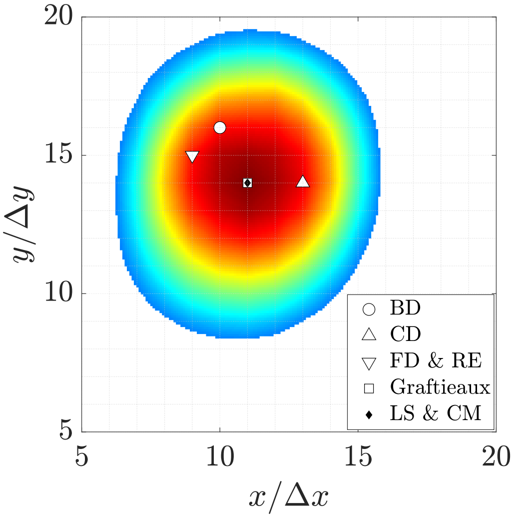

Figure 9. Vortex center locations for different differentiation schemes. The vorticity magnitude contour based on the least squares scheme is shown.

In case of vorticity and Q-criterion employing BD, CD, FD and RE schemes, the estimation of the vortex center is different from the geometrical center of the shape described by the core. As a result the convection velocity also differs significantly between schemes. Figure 10 illustrates the axial and lateral velocities estimated from each VIM and scheme.

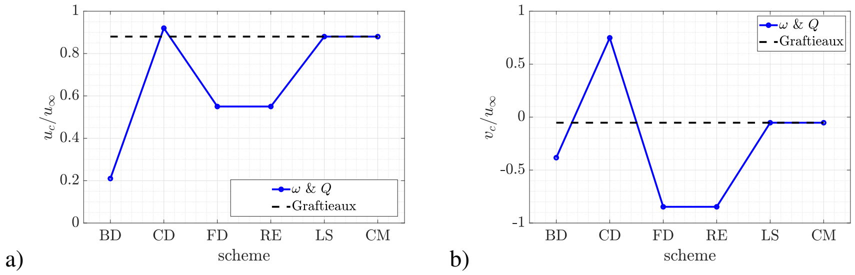

Figure 10. Average convection velocities.

Vorticity and Q-criterion provide the same velocity magnitudes, when the same scheme is applied. In case of CD, LS and CM schemes, the streamwise velocity magnitudes are in good agreement with previous results from Soto-Valle et al. (2020), where the conditional average methodology (van der Wall and Richard, 2006) was implemented with a resulting ratio of $u_c/u_\infty = 0.85$. Conversely, the schemes BD, FD and RE present scattered velocities on both axial and lateral directions. In case of the Graftieaux's VIM, it is independent on the number of neighboring points and the magnitude is close to the smoothest schemes from the other VIMs.

Therefore, the estimation of the convection velocity is recommended with the smoother VIMs and schemes: Graftieaux or vorticity and Q-criterion while employing LS or CM schemes. Alternative methods such as the prediction from time series vortex locations might be also successful using the rest of the schemes due to the small discrepancy between the vortex center locations between VIMs and schemes; however, more than one vortex age is needed.

5.2 Statistical analysis

The vortex center locations are identified on each instantaneous velocity field, which constitutes the complete PIV dataset. In the interest of clarity, only the Graftieaux 24-points as well only vorticity magnitude cases are presented. The reason is due to Graftieaux 8-points and Q-criterion present small differences with the aforementioned cases. For completeness, the full set of results can be found in App. A.

Figure 11 a) shows a contour diagram of the tip vortex center positions obtained through the Graftieaux VIM and the 24-points scheme applied to each velocity field. In fact, the zone can be highlighted as an ellipse that has its main axis on the lateral direction with 5 grid points more than the streamwise direction. Figure 11 b) shows the added up distribution along the streamwise direction.

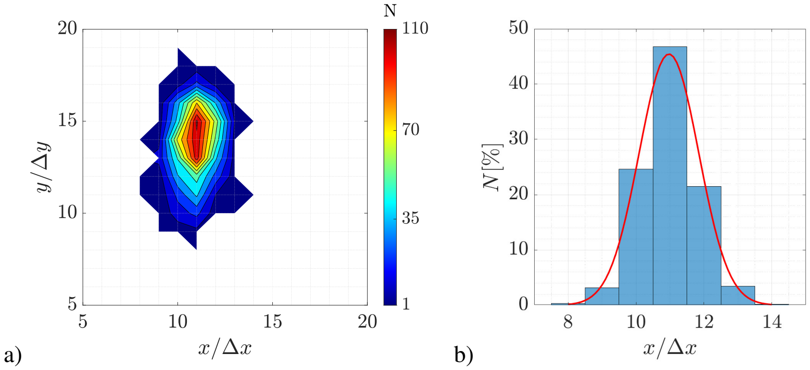

Figure 11. Jittering evaluation using Graftieaux VIM with 24-points scheme. a) contour distribution of the vortex center locations over the area of interest. b) Probability distribution among the streamwise direction.

From Fig. 11, the jittering effect is clearly visible and agrees with previous results from fixed wings (Thompson, 1983; Giuni and Green, 2013b; Bandyopadhyay et al., 1991; Beresh et al., 2010), helicopter rotors (van der Wall and Richard, 2006; Mula et al., 2011) and wind turbines (Maalouf et al., 2009; Soto-Valle et al., 2020; Sherry et al., 2013a). According to these references, the source of the jittering can be varied such as geometry effects, wall boundary layer turbulence, free stream turbulence, surface irregularities or changes in the core structure. Additionally, the vibrations of either the model or the test rig supports can produce small changes in the field of view, resulting in the meandering motion of the vortex. In this way, the jittering in Fig. 11 a) shows the spreading of the vortex center locations with y as a prevalent direction. The probability distribution over the streamwise direction, Fig. 11 b), fits very well with a normal distribution. These characteristics are in agreement with Sherry et al. (2013a), where it is shown that the jittering of the tip vortices in the wake of a horizontal axis wind turbine is predominant in the radial direction compared to the streamwise direction and that at early vortex ages, the normal distribution is a good fit of the tip vortex center distribution. In agreement with the results presented here, Mula et al. (2011) also observed that the jittering of tip vortices generated by helicopter rotors present a preferential direction.

Figure 12 shows the jittering zones for the Graftieaux method and vorticity calculations with the different differentiation schemes. For the purpose of clarity, only ellipse perimeters that contains the 100% of the vortex center locations are presented. It is noticed that the ellipse described by the Graftieaux VIM is thinner in the streamwise direction observing approximately two to four grid steps less than the vorticity VIM, depending on the schemes applied. In fact, the area described by the ellipses on the Graftieaux VIM is 80 ± 6 while in the case of the vorticity and $\boldsymbol{Q}$ are between 145 ± 24, corresponding to an 80% increment. The size variation between schemes in the vorticity VIM, Fig. 12, is more uniform in terms of directions and goes approximately to one grid step in any direction.

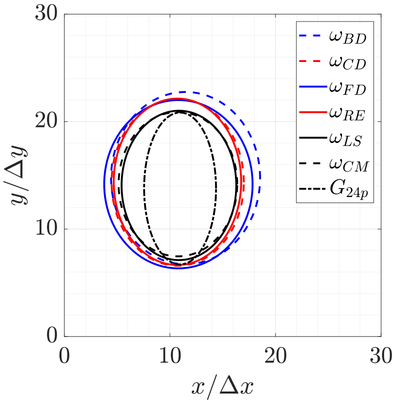

Figure 12. Jittering zones over the area of interest with Graftieaux and vorticity VIMs.

Even though the area swept by the scattering of the estimated vortex center locations are similar in magnitude, in the case of vorticity and $\boldsymbol{Q}$, the probability distribution over these zones differs between the applied schemes. Figure 13 shows the contour diagram of two representative distributions applying vorticity VIM. Hence, Fig. 13 b), which is done with LS scheme, shows a more concentric distribution than CD scheme,Fig. 13 a). Q-criterion and the rest of the schemes exhibit similar results (see App. A).

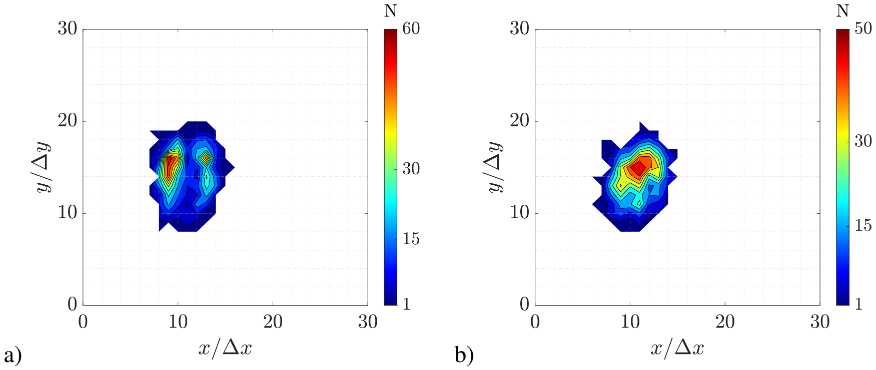

Figure 13. Contour distribution of the vortex center locations over the area of interest from vorticity VIM. a) Central difference scheme. b) Least square scheme.

300 Figure 14 shows the added up distribution towards the streamwise and lateral axes when the vorticity VIM and the CD scheme are applied, together with fitting curves. Each fitting curve is chosen using higher the coefficients of correlation (R^2) between normal, binormal and Weibull distributions. In Fig. 14 a), it can be noticed that the spreading of the vortex centers is over two peaks with a distance of approximately 4 grid points and therefore, a binormal distribution fits better with the data with a coefficient of correlation of $R^2 = 0.99$. In case of the lateral direction, Fig. 14 b), a binormal and Weibull distributions 305 exhibit good fitting, with the coefficients of correlations of $R^2 = 0.97$ and $R^2 = 0.95$, respectively.

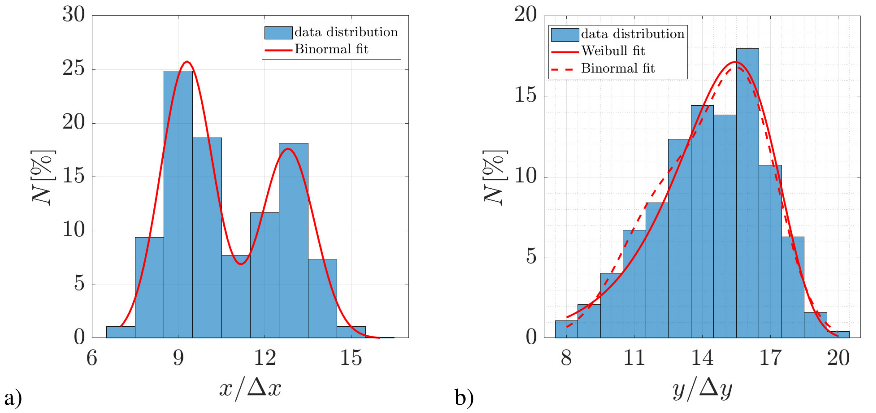

Figure 14. Probability distribution of the vortex center locations using vorticity VIM and CD scheme. Additionally, red lines show fitting curves. a) Streamwise direction. b) Lateral direction.

Figure 15 shows the best-fit curves of the probability distribution when the differentiation schemes BD, CD and LS are applied. In the streamwise direction, Fig. 15 a), the LS scheme presents a normal distribution as the best fit. This is in agreement with the unique maximum observed in the analysis of the average velocity field. Instead, for all the other schemes the binormal distribution is the best fit. The difference is due to the smoothing properties of the LS scheme. In fact, the application is implemented using points up to the two positions farther in the grid, where the outer points are weighted more than the inner ones (see Table 2).

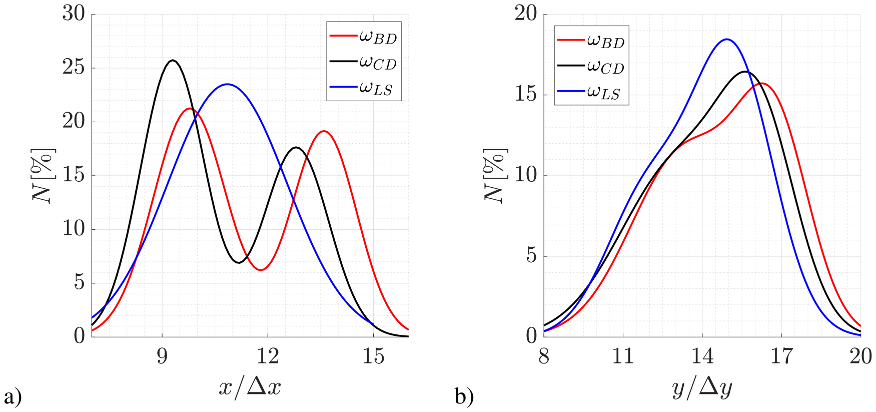

Figure 15. Probability distribution of the vortex center locations while the vorticity VIM is applied using BD, CD and LS schemes. a) Streamwise direction. b) Lateral direction.

Similarly, in the lateral direction, Fig. 15 b), the binormal distribution is likely the best fit with a coefficient of correlation between $0.97 - 0.99$. In this case, peaks are very close, which also gives the Weibull distribution a good fit with coefficients of correlation between $0.95 - 0.97$. In this direction, only one position is concentrated, consequently, the smoothing effect produced by the LS scheme does not have the same effect in this direction.

Overall, the estimation of the vortex center location is influenced by the VIM and scheme. In the same way, the convection velocity and the core radius are affected by the implemented methodology.

To see the effect of the VIM and schemes on the instantaneous convection velocity, Figure 16 shows the normalized convection velocity in the streamwise direction, u_c/u_∞. Each black dot represents the convection velocity estimated through the corresponding VIM and scheme on each velocity field from the PIV dataset. At the same time, the average of the dataset magnitudes is visible as a solid blue line. Moreover, the average value obtained when the methodology was applied on the average velocity field (see Fig. f:03 and Sect. 5) is displayed with a solid red line.

Graftieaux VIM, Fig. 16 a), presents a variation of 10% around its average value (blue line). In the case of the vorticity VIM, Figs. 16 b) and c), the variation increases up to 70% and 33% for the CD and LS schemes, respectively.

Several estimations fail, such as $u_c/u_\infty < 0$ or $u_c/u_\infty > 1$, as well in the average velocity analysis, due to the fact that they are located at the edges of the vortex, i.e., they are highly affected by the induced velocities of the vortex. Figure 17 shows one representative case of instantaneous vorticity where the central scheme is applied. It can be noticed that the highest magnitudes of vorticity are spread from the center of the quiver lines.

However, in the case of Graftieaux, vorticity and Q-criterion (schemes CD, LS and CM), this effect is not prominent and average results have less than 10% error compared with previous estimation $u_c/u_\infty = 0.85$ (Soto-Valle et al., 2020), obtained

https://doi.org/10.5194/wes-2021-104
Preprint. Discussion started: 7 October 2021

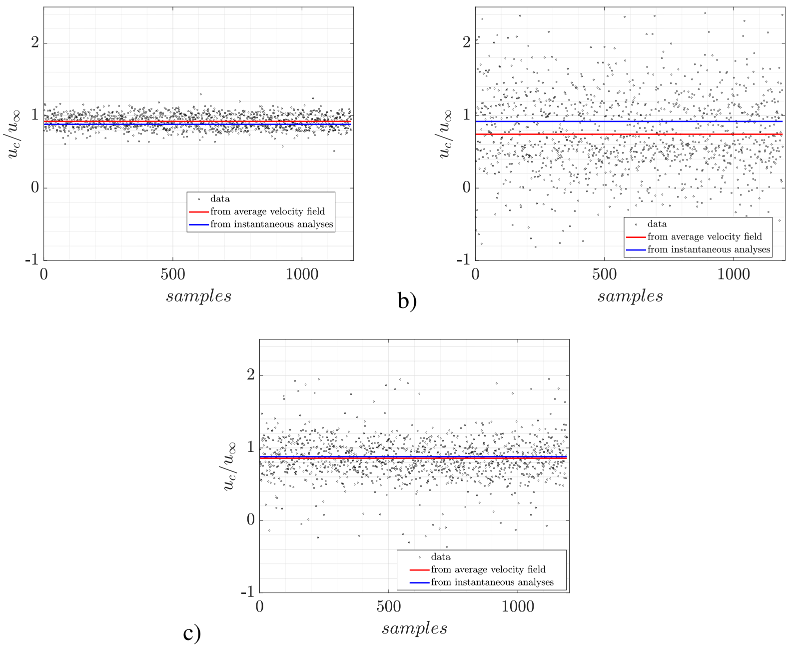

a)

b)

c)

Figure 16. Normalized convection velocity in the streamwise direction. a) Graftieaux. b) Vorticity magnitude, central differentiation scheme. c) Vorticity magnitude, least square scheme.

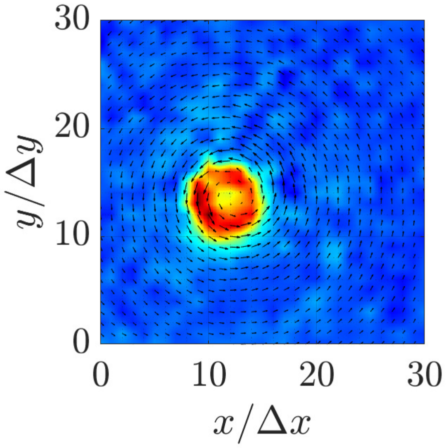

a)

Figure 17. Instantaneous vorticity magnitude with the central differentiation scheme and quiver lines of the velocity field.

through the conditional averaging methodology. This error difference increases between $12-18\%$ in the case of vorticity and Q-criterion (schemes CD, FD and RE) and to more than 50% with the scheme BD.

The visible ring-like concentration on Fig. 17 contrasts the uneven shedding hypothesis from the average results and it leads to the idea of an artifact of the schemes, as it preserves the same ring-like structure even when an instantaneous velocity field is analyzed.

Table 3, shows the full set of average values and their corresponding standard deviations (SD). As discussed, vorticity and Q-criterion yield similar results. Nevertheless, the SD results from Q-criterion are equal or higher than vorticity in all the schemes and in both directions, which is presumable caused by the power of two on its derivatives implementation.

The average convection velocity is also estimated from the average flow field (red line). However, It should be noted that average results must not be overstated because of the tip vortex jittering (van der Wall and Richard, 2006). It is also remarkable how convection velocity has the lowest results from BD scheme and on the contrary, the highest from FD scheme. In fact, both schemes ignore information either forward or backward from the grid on the implementation of differentiation. Therefore, they are not suitable for vortex analysis.

Table 3. Convection velocity magnitudes from the average velocity field and the statistics after instantaneous velocity field analyses.

VIM	scheme	From average velocity field analysis		From instantaneous velocity field analyses		
		u_c/u_∞	v_c/u_∞	$\overline{u_c/u_\infty}$	$\overline{v_c/u_\infty}$	SD
Graftieaux	8-p	0.88	-0.05	0.92	-0.02	0.10-0.13
	24-p	0.88	-0.05	0.92	-0.02	0.10-0.13
Vorticity	BD	0.21	-0.37	0.38	0.46	0.69-0.90
	CD	0.92	0.76	0.74	-0.15	0.53-0.68
	FD	0.55	-0.87	0.95	-0.41	0.64-0.93
	RE	0.55	-0.87	0.72	-0.16	0.59-0.68
	LS	0.88	-0.05	0.86	-0.13	0.28-0.48
	CM	0.88	-0.05	0.82	-0.14	0.41-0.65
Q-criterion	BD	0.21	-0.37	0.4	0.44	0.70-0.92
	CD	0.92	0.76	0.75	-0.16	0.58-0.72
	FD	0.55	-0.87	1.0	-0.37	0.65-0.95
	RE	0.55	-0.87	0.73	-0.14	0.62-0.74
	LS	0.88	-0.05	0.86	-0.13	0.28-0.48
	CM	0.88	-0.05	0.83	-0.15	0.42-0.68

In case of the vortex core radius, even when all the scattering of the convection velocity influences its calculation (see Sect. 4.2) the variation of the radius varies by just a couple of grid steps. In this way, the average values are similar between VIMs and schemes. Figure 18 shows the normalized core radius, $r_c/\Delta x$ when it is estimated through along the horizontal axis. It is found that the results on the vertical axis are slightly higher, by $0.3\Delta x$, which is small enough to assume the vortex as symmetric.

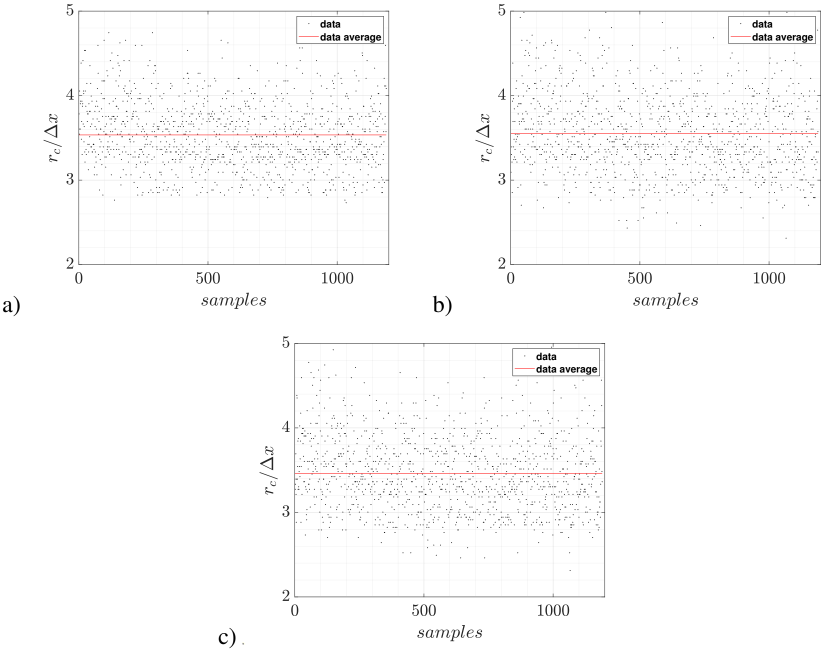

Figure 18. Normalized core radius. a) Graftieaux. b) Vorticity magnitude with CD scheme. c) Vorticity magnitude with LS scheme.

In this way, the magnitude of the core radius is $r_c/\Delta x \approx 3.4$ independently on the VIM and scheme applied. The standard deviation varies between methods; however, it is always lower than $1\Delta x$. This is expected due to the small number of grid points that are found within the core (see Fig. 5). Indeed, the results from the average velocity field are also similar between VIMs and schemes but slightly higher than the statistical results, $r_c/\Delta x \approx 4.4$.

6 Conclusions

Several Vortex Identification Methods (VIMs) and implementation schemes have been applied to the two components of the velocity field data in the near wake of a wind turbine model, obtained through PIV measurements. The methodology was applied to the average velocity field as well as the instantaneous velocities resulting in a statistical analysis of the PIV dataset.

In case of the average flow field, the chosen VIMs and schemes provide different magnitude distributions of the identification parameters. Nevertheless, the vorticity and Q-criterion yield the same estimations of the vortex center locations in all the schemes analyzed. Hence, as long as the vortex is well-formed the vorticity VIM is preferred over the Q-criterion because of the lower standard deviation results.

Through the statistical analysis, it is concluded that different methodologies lead to different interpretations of the tip vortex behavior. Even though the jittering zone is found to be ellipsoidal for all the VIM and schemes, the probability density function of the vortex center locations varies in the streamwise direction from one single peak with the Graftieaux, vorticity and Q (least-squares scheme) to a binormal distribution with the other implementations.

The two peaks found in the jittering are determined as an artifact produced by certain schemes. The latter can be avoided using either Graftieaux VIM or vorticity and Q-criterion while employing the least-squares scheme.

It is concluded that the vortex center locations are within a small variation range and their comparability is viable independently on the VIM or scheme. Nevertheless, first-order schemes, such as backward and forward differences, should be avoided.

The convection velocity presented a higher dependency on the VIM and scheme applied. Therefore, and keeping in mind that the results have shown good comparability regarding the vortex center locations, it is recommended to use the information of several vortex ages instead of the swirling velocity approach to estimate the convection velocity. Conversely, the vortex core radius only showed a grid step variation between VIM and schemes.

Overall, Graftieaux's method is the recommended VIM to track the tip vortex. Indeed, the method does not use differentiation and has shown to be independent of the number of neighboring points used. Moreover, it presents the lowest standard deviation between all the methodologies applied here.

Data availability. Velocity field data and results can be provided by contacting the corresponding author.

Author contributions. RSV carried out the measurement campaign, worked in the methodology, performed calculations and analysis, and wrote the paper. SC implemented and tested the methodology with assistance and supervision from RSV. SC, SB, MM, CNN, AB and COP contributed with comments and discussions about each section in the manuscript.

Competing interests. The authors declare that they have no conflict of interest.

Acknowledgements. This research has been supported by the ANID PFCHA/Becas Chile-DAAD/2016 (grant no. 91645539).

https://doi.org/10.5194/wes-2021-104
Preprint. Discussion started: 7 October 2021

A Appendix

A.1 Jittering zones

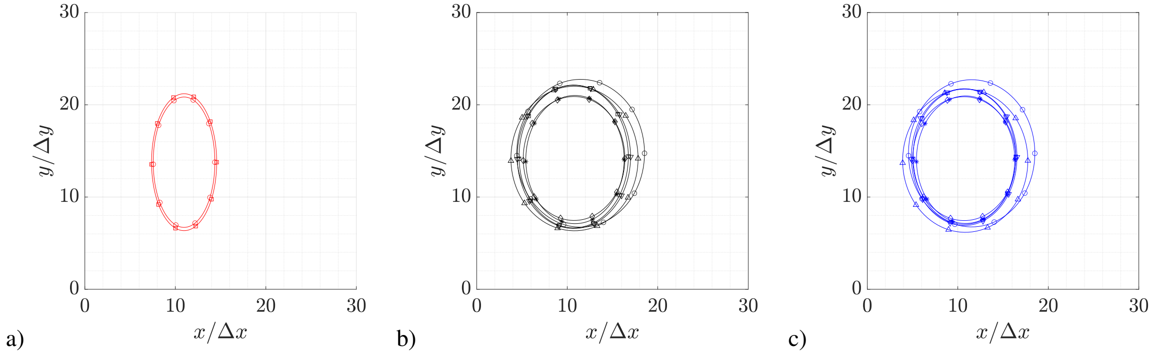

Figure A1. Jittering zone of each VIM and scheme. a) Graftieaux. b) Vorticity magnitude. c) Q-criterion.

385 ## A.2 Probability contours

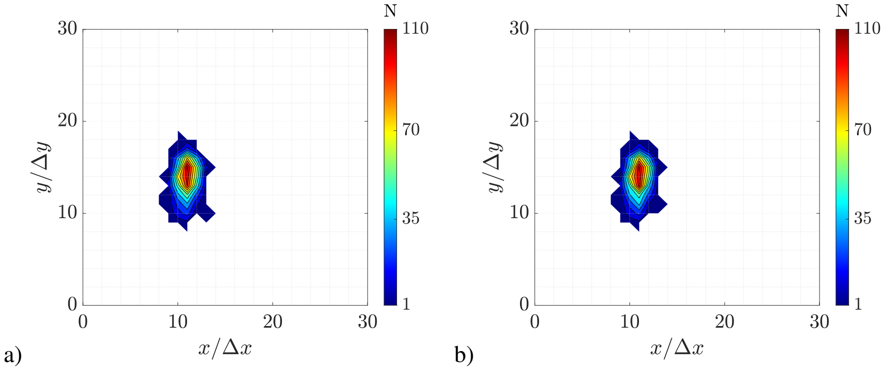

Figure A2. Graftieaux probability contours. a) 8−points. b) 24−points.

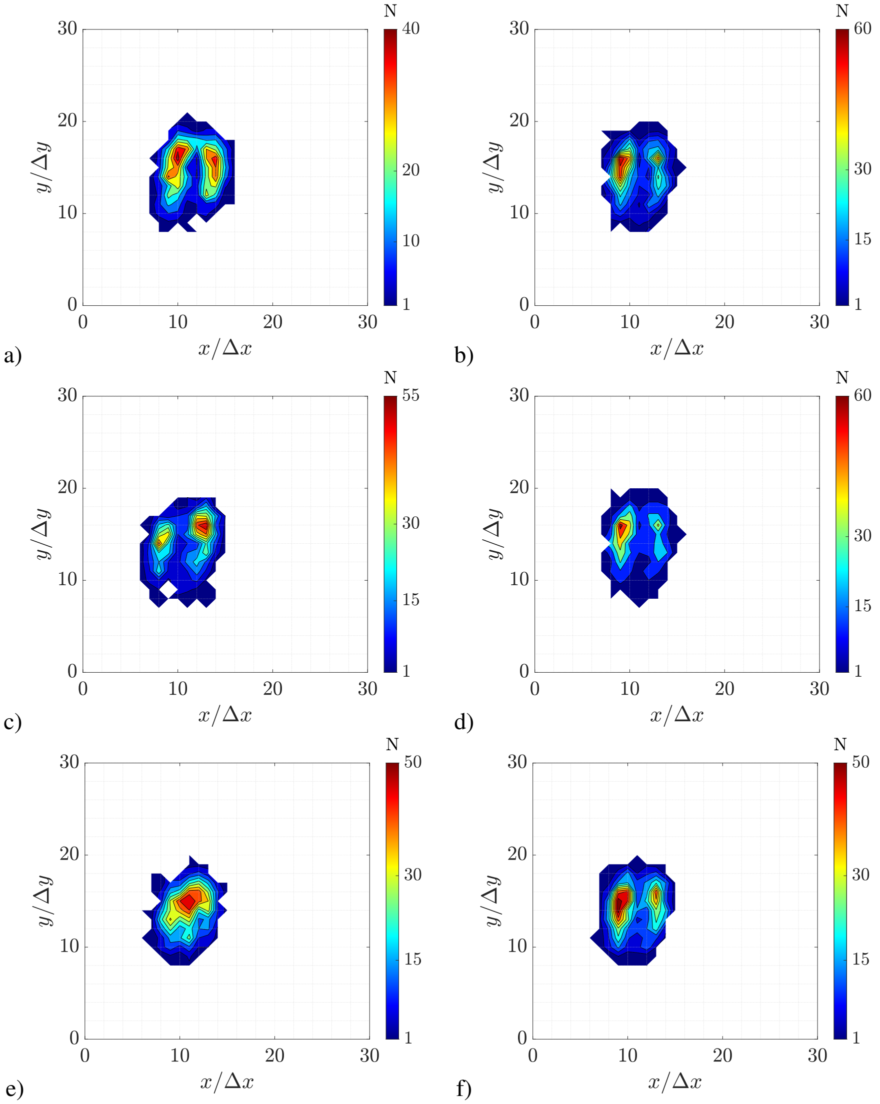

Figure A3. Vorticity probability contours. a) Backward difference. b) Central difference. c) Forward difference. d) Richardson extrapolation. e) Least square. f) Circulation method.

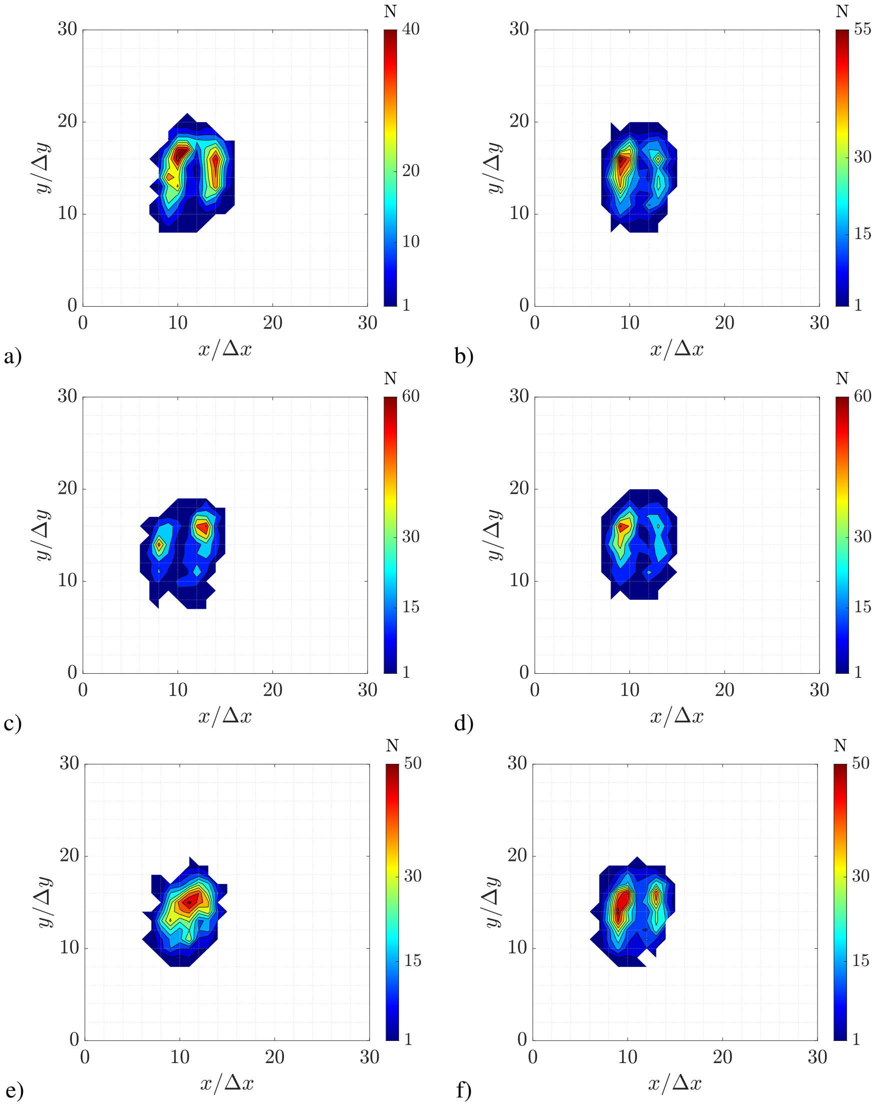

Figure A4. Q-criterion probability contours. a) Backward difference. b) Central difference. c) Forward difference. d) Richardson extrapolation. e) Least square. f) Circulation method.

References

Arakawa, C., Fleig, O., Iida, M., and Shimooka, M.: Numerical approach for noise reduction of wind turbine blade tip with earth simulator, Journal of the Earth Simulator, 2, 11–33, 2005.

Bandyopadhyay, P. R., Stead, D. J., and Ash, R. L.: Organized nature of a turbulent trailing vortex, AIAA journal, 29, 1627–1633, 1991.

Beresh, S. J., Henfling, J. F., and Spillers, R. W.: Meander of a fin trailing vortex and the origin of its turbulence, Experiments in fluids, 49, 599–611, 2010.

Bonnet, J.: Eddy structure identification, Springer, 1998.

Devenport, W. J., Rife, M. C., Liapis, S. I., and Follin, G. J.: The structure and development of a wing-tip vortex, Journal of fluid mechanics, 312, 67–106, 1996.

Foucaut, J.-M. and Stanislas, M.: Some considerations on the accuracy and frequency response of some derivative filters applied to particle image velocimetry vector fields, Measurement Science and Technology, 13, 1058, 2002.

Giuni, M. and Green, R. B.: Vortex formation on squared and rounded tip, Aerospace science and technology, 29, 191–199, 2013a.

Giuni, M. and Green, R. B.: Vortex formation on squared and rounded tip, Aerospace science and technology, 29, 191–199, 2013b.

Graftieaux, L., Michard, M., and Grosjean, N.: Combining PIV, POD and vortex identification algorithms for the study of unsteady turbulent swirling flows, Measurement Science and technology, 12, 1422, 2001.

Hunt, J., Wray, A., and Moin, P.: Eddies, stream, and convergence zones in turbulent flows, in: Proc. Summer Program Center for Turbulence Reserch, Stanford, California, USA, vol. S88, pp. 193–208, Center for Turbulence Research Report, 1988.

Karakus, C., Akilli, H., and Sahin, B.: Formation, structure, and development of near-field wing tip vortices, Proceedings of the Institution of Mechanical Engineers, Part G: Journal of Aerospace Engineering, 222, 13–22, 2008.

Kolář, V.: Vortex identification: New requirements and limitations, International journal of heat and fluid flow, 28, 638–652, 2007.

LeVeque, R. J.: Finite difference methods for differential equations, Draft version for use in AMath, 585, 112, 1998.

Liu, C., Wang, Y., Yang, Y., and Duan, Z.: New omega vortex identification method, Science China Physics, Mechanics & Astronomy, 59, 1–9, 2016.

Liu, C., Gao, Y.-s., Dong, X.-r., Wang, Y.-q., Liu, J.-m., Zhang, Y.-n., Cai, X.-s., and Gui, N.: Third generation of vortex identification methods: Omega and Liutex/Rortex based systems, Journal of Hydrodynamics, 31, 205–223, 2019.

Liu, P.-q., Zhao, Y., Qu, Q.-l., and Hu, T.-x.: Physical properties of vortex and applicability of different vortex identification methods, Journal of Hydrodynamics, 32, 984–996, 2020.

Lourenco, L. and Krothapalli, A.: On the accuracy of velocity and vorticity measurements with PIV, Experiments in fluids, 18, 421–428, 1995.

Maalouf, B., Dobrev, I., and Massouh, F.: Vortex structure in the wake of a wind turbine rotor, in: 19th Congr. Français de Mécanique, Courbevoie, France, 2009.

Marten, D., Paschereit, C. O., Huang, X., Meinke, M., Schroeder, W., Mueller, J., and Oberleithner, K.: Predicting Wind Turbine Wake Breakdown Using a Free Vortex Wake Code, AIAA Journal, 58, 4672–4685, 2020.

Micallef, D.: 3D flows near a HAWT rotor: A dissection of blade and wake contributions, Ph.D. thesis, University of Malta, 2012.

Micallef, D., Akay, B., Sant, T., Ferreira, C. S., and van Bussel, G.: Experimental and numerical study of radial flow and its contribution to wake development of a HAWT, in: Proc. European Wind Energy Association Conf. & Exhibition, Brussels, Belgium, 2011.

Micallef, D., Akay, B., Ferreira, C. S., Sant, T., and van Bussel, G.: The origins of a wind turbine tip vortex, Journal of Physics: Conference Series, 555, 012 074, https://doi.org/10.1088/1742-6596/555/1/012074, 2014.

Mula, S. M., Stephenson, J., Tinney, C. E., and Sirohi, J.: Vortex jitter in hover, in: American helicopter society southwest region technical specialists meeting, Fort Worth, USA, February, pp. 23–25, 2011.

Nilsson, K., Shen, W. Z., Sørensen, J. N., Breton, S.-P., and Ivanell, S.: Validation of the actuator line method using near wake measurements of the MEXICO rotor, Wind Energy, 18, 499–514, 2015.

Ning, Z. and Yang, Z.: An experimental investigation on the control of tip vortices from wind turbine blade, in: 51st AIAA Aerospace Sciences Meeting including the New Horizons Forum and Aerospace Exposition, p. 1104, 2013.

Ostovan, Y., Akpolat, M. T., and Uzol, O.: Experimental Investigation of the Effects of Winglets on the Tip Vortex Behavior of a Model Horizontal Axis Wind Turbine Using Particle Image Velocimetry, J. of Solar Energy Engineering, 141, 011 006, 2019.

Pechlivanoglou, G., Fischer, J., Eisele, O., Vey, S., Nayeri, C., and Paschereit, C.: Development of a medium scale research hawt for inflow and aerodynamic research in the tu berlin wind tunnel, in: 12th German Wind Energy Conf. (DEWEK), Bremen, Germany, 2015.

Raffel, M., Willert, C. E., Scarano, F., Kähler, C. J., Wereley, S. T., and Kompenhans, J.: Particle image velocimetry: a practical guide, Springer, 2018.

Shen, W. Z., Mikkelsen, R., Sørensen, J. N., and Bak, C.: Tip loss corrections for wind turbine computations, Wind Energy: An International Journal for Progress and Applications in Wind Power Conversion Technology, 8, 457–475, 2005.

Sherry, M., Nemes, A., Lo Jacono, D., Blackburn, H. M., and Sheridan, J.: The interaction of helical tip and root vortices in a wind turbine wake, Physics of fluids, 25, 117 102, 2013a.

Sherry, M., Sheridan, J., and Jacono, D. L.: Characterisation of a horizontal axis wind turbine's tip and root vortices, Experiments in fluids, 54, 1417, 2013b.

Shkarayev, S. V. and Kurnosov, V.: Modification of vortex identification method based on normalized angular momentum, in: 33rd AIAA Aerodynamic Measurement Technology and Ground Testing Conference, p. 3556, 2017.

Skinner, S., Green, R., and Zare-Behtash, H.: Wingtip vortex structure in the near-field of swept-tapered wings, Physics of Fluids, 32, 095 102, 2020.

Smith, G., Grant, I., Liu, A., and Infield, D.: Diagnostics of Wind-Turbine Aerodynamics by Particle Image Velocimetry, in: Wind Energy Conversion 1990: Proceedings of the 12th BWEA Conference, Norwich, March 1990, pp. 259–64, 1990.

Snel, H., Schepers, J., and Montgomerie, B.: The MEXICO project (Model Experiments in Controlled Conditions): The database and first results of data processing and interpretation, in: Journal of Physics: Conference Series, vol. 75, p. 012014, IOP Publishing, 2007.

Soto-Valle, R., Alber, J., Manolesos, M., Nayeri, C. N., and Paschereit, C. O.: Wind Turbine Tip Vortices under the influence of Wind Tunnel Blockage Effects, Journal of Physics: Conference Series, 1618, 032 045, https://doi.org/10.1088/1742-6596/1618/3/032045, 2020.

Spalart, P. R.: Direct simulation of a turbulent boundary layer up to R θ= 1410, Journal of fluid mechanics, 187, 61–98, 1988.

Thompson, D.: A flow visualisation study to tip vortex formation, Tech. rep., AERONAUTICAL RESEARCH LABS MELBOURNE (AUSTRALIA), 1983.

van der Wall, B. G. and Richard, H.: Analysis methodology for 3C-PIV data of rotary wing vortices, Experiments in Fluids, 40, 798–812, 2006.

Vétel, J., Garon, A., and Pelletier, D.: Vortex identification methods based on temporal signal-processing of time-resolved PIV data, Experiments in fluids, 48, 441–459, 2010.

Whale, J., Anderson, C., Bareiss, R., and Wagner, S.: An experimental and numerical study of the vortex structure in the wake of a wind turbine, Journal of Wind Engineering and Industrial Aerodynamics, 84, 1–21, 2000.

Yamauchi, G. K., Burley, C. L., Mercker, E., Pengel, K., and JanakiRam, R.: Flow measurements of an isolated model tilt rotor, Tech. rep., NATIONAL AERONAUTICS AND SPACE ADMINISTRATION MOFFETT FIELD CA AMES RESEARCH . . . , 1999.

Yang, Z., Sarkar, P., and Hu, H.: An experimental investigation on the wake characteristics of a wind turbine in an atmospheric boundary layer wind, in: Proc. 29th American Institute of Aeronautics and Astronautics Applied Aerodynamics Conf. Honolulu, Hawaii, USA, p. 3815, 2011.

Yang, Z., Sarkar, P., and Hu, H.: Visualization of the tip vortices in a wind turbine wake, J. of visualization, 15, 39–44, 2012.

Zhang, Y., Liu, K., Xian, H., and Du, X.: A review of methods for vortex identification in hydroturbines, Renewable and Sustainable Energy Reviews, 81, 1269 – 1285, https://doi.org/https://doi.org/10.1016/j.rser.2017.05.058, 2018a.

Zhang, Y.-n., Qiu, X., Chen, F.-p., Liu, K.-h., Dong, X.-r., and Liu, C.: A selected review of vortex identification methods with applications, Journal of Hydrodynamics, 30, 767–779, 2018b.